



Discovery of a reversible redox-induced order-disorder transition in a 10-component compositionally complex ceramic

Dawei Zhang^a, Yan Chen^b, Tianshi Feng^c, Dunji Yu^b, Ke An^b, Renkun Chen^{a,c}, Jian Luo^{a,e,*}

^a Program of Materials Science and Engineering, University of California San Diego, La Jolla, CA, 92093, USA

^b Neutron Scattering Division, Oak Ridge National Laboratory, Oak Ridge, TN, 38731, USA

^c Department of Mechanical & Aerospace Engineering, University of California San Diego, La Jolla, CA, 92093, USA

^e Department of NanoEngineering, University of California San Diego, La Jolla, CA, 92093, USA

ARTICLE INFO

Keywords:

Redox phase transition
Order-disorder transition
Compositionally complex ceramic
High-entropy oxide
Fluorite

ABSTRACT

This study discovers a reversible order-disorder transition (ODT) in a 10-component compositionally complex ceramic, $(\text{Nd}_{0.15}\text{Pr}_{0.15}\text{Dy}_{0.8}\text{Ho}_{0.8}\text{Er}_{0.8}\text{Ti}_{0.2}\text{Yb}_{0.1}\text{Hf}_{0.1}\text{Zr}_{0.1}\text{Nb}_{0.8})\text{O}_{7-8}$, induced via annealing in oxidized vs. reduced environments at 1600 °C. Notably, the 10-cation oxide remains a homogenous single-phase high-entropy solid solution before and after the ODT in the pyrochlore vs. fluorite structure that can be quenched. *In-situ* neutron diffraction reveals the oxygen vacancy formation and atomic displacement during this ODT. This study reveals a new pathway to induce ODT via a redox transition to tailor the properties of compositionally complex fluorite-based oxides.

Disorder and order in fluorite-based oxides can influence on a range of physical properties. For example, disorder can increase the ionic conductivities of yttria-stabilized zirconia (YSZ) and $\text{Y}_2(\text{Zr}_y\text{Ti}_{1-y})_2\text{O}_7$ [1, 2], enhance the catalytic activity and stability of Li-O₂ batteries [3], and tailor the radiation resistance [4,5]. Long- or short-range pyrochlore and weberite orders can also exist in fluorite-based oxides [6]. The $\text{A}_2\text{B}_2\text{O}_7$ pyrochlore structure can be viewed as a $2 \times 2 \times 2$ superstructure of a base fluorite structure with ordered cations and oxygen vacancies and structural distortion [7]. Prior studies showed that the pyrochlore can transit to a defect fluorite structure, caused by composition [8–15] or temperature [16] induced disorder. In this work, we have further discovered a reversible redox-induced transition between the ordered pyrochlore and disordered fluorite structures.

In 2018, Gild et al. reported several single-phase YSZ-like high-entropy fluorite oxides (e.g., $(\text{Zr}_{1/5}\text{Hf}_{1/5}\text{Ce}_{1/5}\text{Y}_{1/5}\text{Yb}_{1/5})\text{O}_{2-8}$ and $(\text{Zr}_{1/5}\text{Hf}_{1/5}\text{Ce}_{1/5}\text{Y}_{1/5}\text{Gd}_{1/5})\text{O}_{2-8}$) with high cation disorder and reduced thermal conductivities [17]. Since then, high-entropy fluorite oxides [10,17–23] (including rare-earth niobates RE_3NbO_7 in the defect fluorite structure [10,20–23]) and fluorite-based pyrochlore oxides [10,18, 24–28] have been investigated for potential applications in thermal barrier coatings (TBCs). These high-entropy fluorite and pyrochlore oxides [10,18,28,20–27] belong to a broader class of high-entropy ceramics (HECs) that have attracted increasing research interests [29],

which also include high-entropy rocksalt [30] and perovskite [31] oxides, borides (of MB_2 [32], MB [33], M_3B_4 [34], MB_4 [35], and MB_6 [36, 37] stoichiometries), silicides (of MSi_2 [38] and M_5Si_3 [39] stoichiometries), and carbides [40–42]. To date, most HEC studies are focused on equimolar compositions consisting of typically five (and sometimes four or six) metal cations.

In 2020, it was further proposed to broaden HECs to compositionally complex ceramics (CCCs) to include non-equimolar compositions that can outperform their equimolar counterparts [29,43]. Moreover, compositionally complex fluorite-based oxides (CCFBOs) can also possess point defects (oxygen vacancies and aliovalent cations) and short- and long-range orders, which provide additional dimensions to tailor their thermomechanical properties [10,18,29,43]. Notably, a recent study reported a series of 11-cation single-phase CCFBOs with a composition-induced order-disorder (pyrochlore-fluorite) transition [10]. In a broad perspective, order and disorder can affect (or even control) many thermal and mechanical properties. However, it is not yet demonstrated that an order-disorder transition (ODT) can take place in a CCFBO (or any CCC and HEC in general) of a fixed composition.

In this study, we design a 10-cation oxide $(\text{Nd}_{0.15}\text{Pr}_{0.15}\text{Dy}_{0.8}\text{Ho}_{0.8}\text{Er}_{0.8}\text{Ti}_{0.2}\text{Yb}_{0.1}\text{Hf}_{0.1}\text{Zr}_{0.1}\text{Nb}_{0.8})\text{O}_{7-8}$. This composition is obtained by mixing 20% of a compositionally complex pyrochlore oxide $[(\text{Nd}_{0.375}\text{Pr}_{0.375}\text{Yb}_{0.25})_2(\text{Ti}_{0.5}\text{Hf}_{0.25}\text{Zr}_{0.25})_2\text{O}_7]$ with 80% of

* Corresponding author.

E-mail address: jluo@alum.mit.edu (J. Luo).

<https://doi.org/10.1016/j.scriptamat.2022.114699>

Received 22 November 2021; Received in revised form 12 March 2022; Accepted 21 March 2022

1359-6462/© 2022 The Author(s). Published by Elsevier Ltd on behalf of Acta Materialia Inc. This is an open access article under the CC BY license (<http://creativecommons.org/licenses/by/4.0/>).

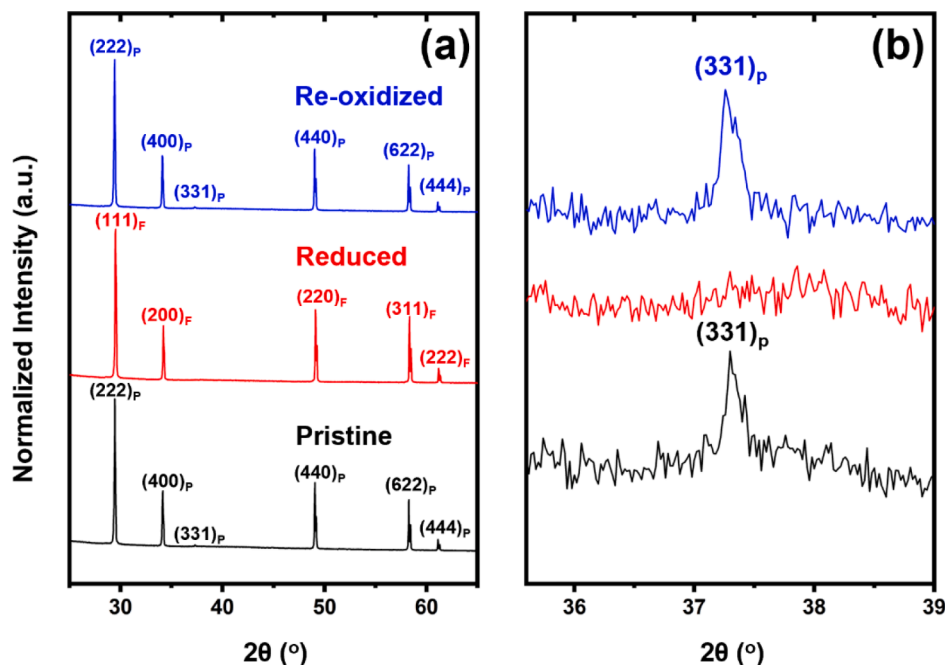


Fig. 1. XRD patterns of (a) the pristine (synthesized in air), reduced, and re-oxidized specimens, and (b) an enlarged region showing the pyrochlore (331) superstructure peaks. The pristine sample was sintered in air at 1600 °C, which was then annealing at 1600 °C in vacuum (the reduced specimen) and subsequently in air at 1600 °C (the re-oxidized specimen). Here, the pyrochlore (222)_P peak corresponds to the fluorite (111)_F peak, where we use subscript “P” and “F” to denote the phase.

a high-entropy (fluorite-structured) rare-earth niobate [(DyHoErNb)_{0.7}O₇]. The mixture forms a single-phase pyrochlore structure when it is synthesized in air, with the nominal formula: (Pr_{0.075}Nd_{0.075}Dy_{0.4}Ho_{0.4}Er_{0.05})₂(Ti_{0.1}Zr_{0.05}Hf_{0.05}Nb_{0.4}Er_{0.35}Yb_{0.05})₂O₇ (with smaller cations on the B sites, albeit anti-site defects; see Supplementary Discussion). We denote this 10-cation CCFBO as “10CCFBO_{0.8Nb}” for brevity, where the subscript denotes the Nb (or niobate) content. The composition of this 10CCFBO_{0.8Nb} is selected so that it is a barely ordered pyrochlore phase (as it would become a disordered defect fluorite structure in air if we further increased the Nb or fluorite-structured niobate content). This composition design enables us to explore a disordering transition induced by oxygen vacancy generation under a reduced environment, which has not been reported previously, to explore a new route to tailor the order/disorder and properties of CCFBOs (or CCCs in general).

All powders were purchased (from US Research Nanomaterials Inc., Houston, TX), ball milled, and uniaxially pressed into pellets, which were subsequently sintered at 1600 °C for 24 h in air (following a standard recipe described in a prior report [10]). Specimen densities were measured by the Archimedes method to be ~98% of the theoretical density. We use “pristine” 10CCFBO_{0.8Nb} to refer to (oxidized) as-sintered samples. The pristine 10CCFBO_{0.8Nb} was annealed at 1600 °C for 2 h in vacuum (10⁻³ mbar) in a graphite furnace (RED DEVIL, RD WEBB, Cambridge, MA) to reduce it to induce an ODT. Subsequently, we

re-annealed a reduced 10CCFBO_{0.8Nb} in air at 1600 °C for 12 h to re-oxidize it to check whether the ODT is reversible. Specimens were characterized by using X-ray diffraction (Miniflex II XRD, Rigaku), a field emission scanning electron microscope (FE SEM, FEI Apero) in conjunction with energy dispersive X-ray spectroscopy (EDS), and an aberration-corrected scanning transmission electron microscope (STEM, JEOL 300CF) in conjunction with EDS and electron energy loss spectroscopy (EELS). Furthermore, *in-situ* heating neutron diffraction in a vacuum furnace up to 1600 °C was carried out at the VULCAN diffractometer [44], Spallation Neutron Source (SNS) at the Oak Ridge National Laboratory (ORNL). The details of the neutron diffraction experiments and Rietveld refinements can be found in the Supplementary Note. Laser flash analysis (LFA 467 HT HyperFlash, NETZSCH) was used to measure thermal diffusivity and subsequently calculate the thermal conductivity (*k*) using the measured density and estimated heat capacity (following a commonly used procedure described previously [10,18]). See Supplementary Note for details of the thermal conductivity measurements and a transparent model that was used to exclude the contribution of radiation heat transfer at high temperatures for more accurate measurement of thermal conductivity.

XRD patterns of the pristine, reduced, and re-oxidized specimens showed a reversible redox-induced ODT between ordered pyrochlore and disordered fluorite structures (Fig. 1). All three XRD patterns suggested the formation of a single phase (without any detectable

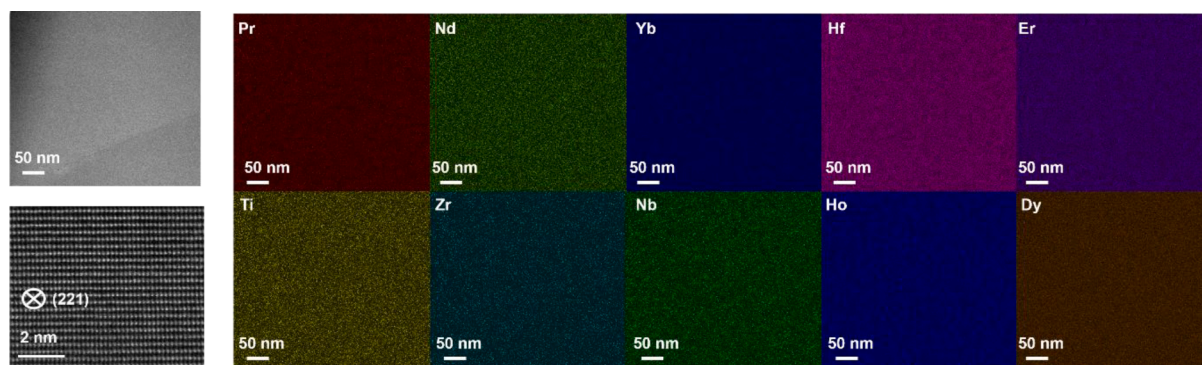


Fig. 2. STEM HAADF images and nanoscale EDS elemental mapping of the pristine 10CCFBO_{0.8Nb}, showing the structural and compositional homogeneity.

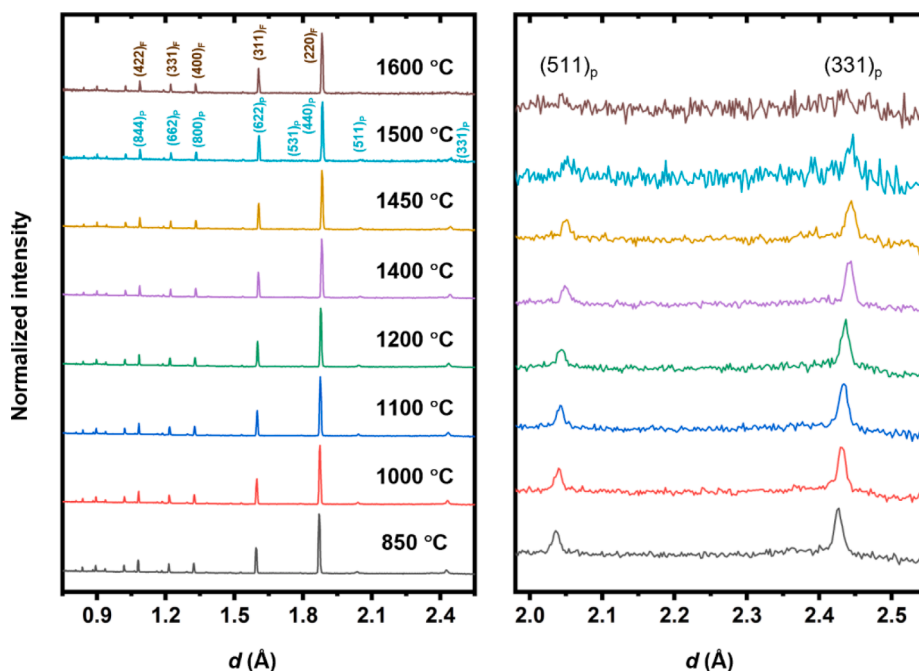


Fig. 3. In-situ heating (reduction) neutron diffraction patterns collected at different temperatures in vacuum and the enlarged region showing the pyrochlore (331) and (511) superstructure peaks. The peak shift was induced by thermal expansion.

secondary phase, as shown in Fig. 1) in each case. SEM EDS elemental mapping was used to confirm the compositional homogeneity in all three specimens (Supplementary Fig. S1). The pyrochlore and fluorite phases can be differentiated by the (331) superstructure peak, which were clearly evident for the pristine and re-oxidized specimens, but not detectable in the reduced specimen. Similar to the cases of weakly ordered $Gd_2Zr_2O_7$ [16,45], the pyrochlore superstructure peaks in the pristine and re-oxidized 10CCFBO_{0.8Nb} were weak because they were barely ordered. We also noticed a reversible color change. As shown in the Supplementary Fig. S2, both the pristine and re-oxidized specimens were brown, but the reduced sample was black (presumably due to the formation of oxygen vacancies). The reduced sample was cross sectioned, grinded, and polished to confirm the color change (reduction) was uniform throughout the whole pellet. The atomic level structure and nanoscale compositional homogeneity were checked and verified by STEM HAADF imaging and EDS elemental mapping (Fig. 2). We also conducted EELS in STEM to probe the O K edge but only observed a small shift in the reduced specimen (Supplementary Fig. S3) that might

be attributed to the reduction (albeit specimen preparation artifacts). In summary, the pristine specimen sintered in air at 1600 °C was ordered pyrochlore, which underwent an ODT to form a disordered defect fluorite phase after reduction at 1600 °C and transformed back to the ordered pyrochlore phase after re-oxidation at 1600 °C.

Prior studies suggested that disordering of $A_2B_2O_7$ pyrochlore can be induced by altering ratio of ionic radii ($r_{A^{3+}}/r_{B^{4+}} < \sim 1.46$ for ternary oxides [8]) or increasing temperature (e.g., in weakly ordered $Gd_2Zr_2O_7$ [16]). In this study, we hypothesize a new redox-induced ODT mechanism where the observed reduction-induced disordering is attributed to the formation of the oxygen vacancies. Here, *ex-situ* benchtop XRD is insufficient to understand this new mechanism. Neutron diffraction can be used to probe structural changes with higher precisions [46–49], including those in high-entropy pyrochlores [50]. Thus, we conducted *in-situ* neutron diffraction experiments at the Vulcan station at the ORNL SNS. Specifically, we heated a pristine (oxidized) specimen in a vacuum furnace with a stepwise heating profile and collected neutron diffraction patterns at 850 °C, 1000 °C, 1100 °C, 1200 °C, 1400 °C, 1450 °C, 1500

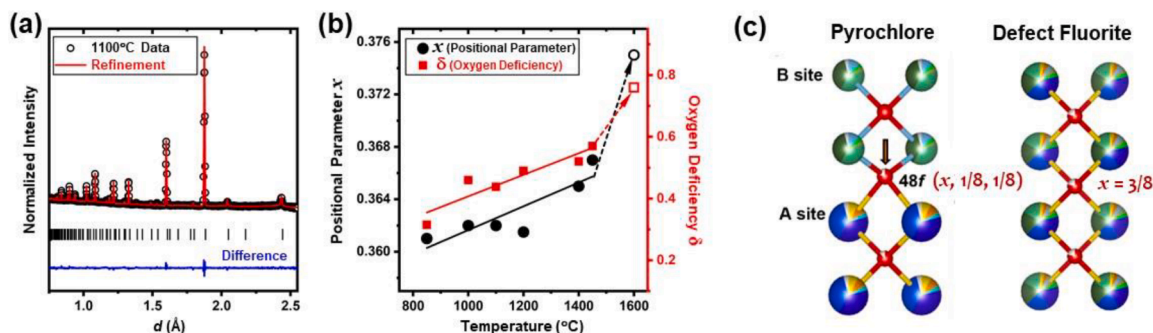


Fig. 4. (a) An example of the Rietveld refinement of the neutron diffraction pattern (for the measurement at 1100 °C). The fitting error $wR_p \approx 2.5\%$. Additional cases are shown in the Supplementary Fig. S4. (b) Evolution of positional parameter x and oxygen deficiency δ vs. temperature, obtained via Rietveld refinements. The solid symbols were the values refined with the pyrochlore structure and the hollow ones were refined assuming the fluorite structure. The solid lines represent the best fittings for the pyrochlore structures while the dashed lines suggest the transition with the ODT. (c) Comparison of (the relevant sections of) pyrochlore and defect fluorite structures. In an ODT, the 48f oxygen, which is located at the position $(x, 1/8, 1/8)$ in the ordered pyrochlore structure, moves gradually along the direction label by the arrow ($x \rightarrow 3/8$) to the position $(3/8, 1/8, 1/8)$ in the defect fluorite structure. See full information of the $A_2B_2O_7$ pyrochlore structure and the positions of different atoms (A, B and O). Note that oxygen (O) anions in Supplementary Fig. S9.

°C, and 1600 °C in a sequence. During heating, the gas pressure was kept at 10^{-5} mbar to produce a reduced environment. Fig. 3 shows the *in-situ* neutron diffraction patterns with an enlarged region showing the pyrochlore (331) and (511) superstructure peaks. With increasing temperature, the superstructure peaks gradually broadened; they completely vanished at 1600 °C, indicating a reduction-induced disordering transition (ODT) to form a defect fluorite structure.

Rietveld refinements were conducted to fit the neutron patterns. For the $A_2B_2O_7$ pyrochlore (Fd $\bar{3}m$) structure, we assume that Yb^{3+} and parts of Er^{3+} cations occupy the B site based on the ionic radii (by placing smaller cations on B sites, while maintaining the exact A:B stoichiometry) and the Rietveld refinement fittings (discussed in detail in Supplementary Discussion) so that the pyrochlore chemical formula is $(Pr_{0.075}Nd_{0.075}Dy_{0.4}Ho_{0.4}Er_{0.05})_2(Ti_{0.1}Zr_{0.05}Hf_{0.05}Nb_{0.4}Er_{0.35}Yb_{0.05})_2O_{7-\delta}$. For the disordered fluorite (Fm $\bar{3}m$) phase (for 1600 °C data only), all cations occupy at the same sublattice with the formula $(Nd_{0.15}Pr_{0.15}Dy_{0.8}Ho_{0.8}Er_{0.8}Ti_{0.2}Yb_{0.1}Hf_{0.1}Zr_{0.1}Nb_{0.8})O_{7-\delta}$. With these schemes, the refinement errors were lowered down to $wR_p \approx 0.025$. One fitting example is given in Fig. 4(a) and other refinement patterns are documented in Supplementary Fig. S4. In addition to the normal refinement parameters, two major parameters considered here were positional parameter x of the O1 (48f) site (at the position x , 1/8, 1/8) in the pyrochlore unit cell and the oxygen deficiency δ (that is determined by the occupancies of the three oxygen sites for the pyrochlore structure, as documented and discussed in Supplementary Table S2). As shown in prior reports [1,10], the positional parameter x of the O1 site will move to 0.375 in an ideal pyrochlore to fluorite ODT. The main fitted parameters of refinements are shown in Supplementary Table S2.

Fig. 4(b) plots the fitted positional parameter x and oxygen deficiency δ vs. temperature. With increasing temperature, both x and δ increase. These trends are consistent with prior investigations of the compositionally induced ODT in $Y_2(Ti_yZr_{1-y})_2O_7$ with increasing y [1,2]. Here, in addition to the displacement of the O1 site (changing of x), there are increases in oxygen deficiency. Our *in-situ* neutron experiments suggest that the positional parameter x of the O1 site approaches ~ 0.367 and oxygen deficiency δ reaches a significant value of ~ 0.57 , just before the ODT. Here, the average occupancy of the oxygen sites (~ 0.80 ; see Supplementary Table S2) is significantly below the nominal value of 0.875 in the defect fluorite structure, creating a large driving force for disordering. A schematic of oxygen migration in an ODT was shown in Fig. 4(c), where the 48f oxygen located at the position (x , 1/8, 1/8) in

the ordered pyrochlore structure moves gradually to the position (3/8, 1/8, 1/8) in the defect fluorite structure.

The thermal diffusivity was measured using a Laser Flash Analyzer (LFA 467 HT HyperFlash, NETZSCH, Germany). All measurements were conducted from room temperature (25 °C) up to 1000 °C in an Ar gas environment, with five individual measurements at each temperature point. Due to the direct radiative heat transfer through the sample at high temperature, a transparent model was used to fit the raw LFA data to extract the thermal diffusivity by including the radiative heat transfer term in the boundary conditions while neglecting the internal photon emission and absorption. The model and the fitting results are shown in detail in Supplementary Note and Fig. S5. Fig. 5 shows that both ordered pyrochlore and disordered fluorite 10CCFBO $_{0.8Nb}$ exhibit low thermal conductivities and amorphous-like temperature dependence (increasing thermal conductivity at higher temperature). The disordered fluorite 10CCFBO $_{0.8Nb}$ has a slightly higher room temperature thermal conductivity of $\sim 1.14 \text{ W}\cdot\text{m}^{-1}\cdot\text{K}^{-1}$ (vs. $\sim 1.11 \text{ W}\cdot\text{m}^{-1}\cdot\text{K}^{-1}$ for ordered pyrochlore 10CCFBO $_{0.8Nb}$) and similar slope with increasing temperature. At 600 °C, the disordered fluorite 10CCFBO $_{0.8Nb}$ also maintains a slightly higher thermal conductivity of $\sim 1.24 \text{ W}\cdot\text{m}^{-1}\cdot\text{K}^{-1}$, compared to $\sim 1.22 \text{ W}\cdot\text{m}^{-1}\cdot\text{K}^{-1}$ for the ordered pyrochlore 10CCFBO $_{0.8Nb}$. XRD characterization after the thermal conductivity measurements in Ar up to 1000 °C showed that the measurements did not change the pyrochlore vs. fluorite structures of these two specimens (Supplementary Fig. S8). In other words, the order vs. disordered structure obtained via redox at 1600 °C can be quenched and preserved during thermal cycling from room temperature to 1000 °C, which offered a unique opportunity to investigate the effects of order vs. disorder on thermal conductivity on specimens of an identical composition.

In summary, we have discovered a reversible redox-induced pyrochlore-to-fluorite transition in a 10-cation CCFBO from the ordered pyrochlore to the disordered fluorite structure, while maintaining a single high-entropy solid solution phase before and after this ODT. *In-situ* neutron diffraction revealed that this ODT is induced by the generation of oxygen vacancies. An ODT can alter the physical properties, e. g., thermal conductivity; specifically, the disordered fluorite 10CCFBO $_{0.8Nb}$ has a slightly higher thermal conductivity than the ordered pyrochlore 10CCFBO $_{0.8Nb}$ from room temperature to 600 °C.

Declaration of Competing Interest

The authors declare that they have no known competing financial interests or personal relationships that could have appeared to influence the work reported in this paper.

Acknowledgment

The work is supported by the National Science Foundation (NSF) in the Ceramics program via Grant No. DMR-2026193. A portion of this research used resources at the Spallation Neutron Source, a DOE Office of Science User Facility operated by the ORNL. The FIB and STEM work utilized the shared facilities at the San Diego Nanotechnology Infrastructure of UCSD, a member of the National Nanotechnology Coordinated Infrastructure (supported by the NSF ECCS-1542148) and the Irvine Materials Research Institute (through UCI CCAM, partially supported by NSF DMR-2011967).

Supplementary materials

Supplementary material associated with this article can be found, in the online version, at doi:10.1016/j.scriptamat.2022.114699.

References

- [1] S.T. Norberg, S. Hull, S.G. Eriksson, I. Ahmed, F. Kinyanjui, J.J. Biendicho, *Chem. Mater.* 24 (2012) 4294–4300.

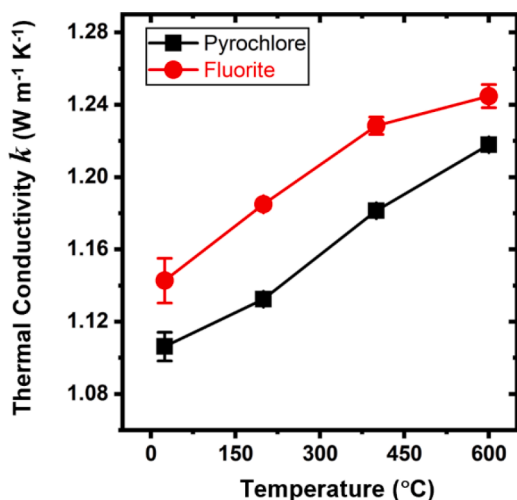


Fig. 5. Temperature-dependent thermal conductivities of the ordered (pyrochlore) vs. disordered (fluorite) specimens of an identical composition. XRD measurements (Supplementary Fig. S8) showed the ordered (pyrochlore) vs. disordered (fluorite) structure can be maintained during the measurements up to 1000 °C. The error bars were standard deviations from five measurements at each temperature.

- [2] C. Heremans, B.J. Wuensch, J.K. Stalick, E. Prince, J. Solid State Chem. 117 (1995) 108–121.
- [3] S.H. Oh, R. Black, E. Pomerantseva, J.H. Lee, L.F. Nazar, Nat. Chem. 4 (2012) 1004–1010.
- [4] K.E. Sickafus, L. Minervini, R.W. Grimes, J.A. Valdez, M. Ishimaru, F. Li, K. J. McClellan, T. Hartmann, Science (80-) 289 (2000) 748–751.
- [5] K.E. Sickafus, R.W. Grimes, J.A. Valdez, A. Cleave, M. Tang, M. Ishimaru, S. M. Corish, C.R. Stanek, B.P. Uberuaga, Nat. Mater. 63 (6) (2007) 217–223, 2007.
- [6] J. Shamblyn, C.L. Tracy, R.I. Palomares, E.C. O'Quinn, R.C. Ewing, J. Neuefeind, M. Feyngenson, J. Behrens, C. Trautmann, M. Lang, Acta Mater 144 (2018) 60–67.
- [7] M.A. Subramanian, G. Aravamudan, G.V. Subba Rao, Prog. Solid State Chem. 15 (1983) 55–143.
- [8] A.F. Fuentes, S.M. Montemayor, M. Maczka, M. Lang, R.C. Ewing, U. Amador, Inorg. Chem. 57 (2018) 12093–12105.
- [9] C. Wan, Z. Qu, A. Du, W. Pan, J. Am. Ceram. Soc. 94 (2011) 592–596.
- [10] A.J. Wright, Q. Wang, C. Hu, Y.T. Yeh, R. Chen, J. Luo, Acta Mater 211 (2021), 116858.
- [11] Y.H. Lee, H.S. Sheu, J.P. Deng, H.C.I. Kao, J. Alloys Compd. 487 (2009) 595–598.
- [12] Y. Liu, R.L. Withers, L. Norén, J. Solid State Chem. 177 (2004) 4404–4412.
- [13] D.L. Drey, E.C. O'Quinn, T. Subramani, K. Lilova, G. Baldinozzi, I.M. Gussev, A. F. Fuentes, J.C. Neuefeind, M. Everett, D. Sprouster, A. Navrotsky, R.C. Ewing, M. Lang, RSC Adv. 10 (2020) 34632–34650.
- [14] D. Drey, E. O'Quinn, S. Finkeldei, J. Neuefeind, M. Lang, Acta Mater 225 (2021), 117590.
- [15] E.C. O'quinn, K.E. Sickafus, R.C. Ewing, G. Baldinozzi, J.C. Neuefeind, M. G. Tucker, A.F. Fuentes, D. Drey, M.K. Lang, Sci. Adv 6 (2020).
- [16] L. Zhou, Z. Huang, J. Qi, Z. Feng, D. Wu, W. Zhang, X. Yu, Y. Guan, X. Chen, L. Xie, K. Sun, T. Lu, Metall. Mater. Trans. A 471 (47) (2015) 623–630, 2015.
- [17] J. Gild, M. Samiee, J.L. Braun, T. Harrington, H. Vega, P.E. Hopkins, K. Vecchio, J. Luo, J. Eur. Ceram. Soc. 38 (2018) 3578–3584.
- [18] A.J. Wright, Q. Wang, S.-T. Ko, K.M. Chung, R. Chen, J. Luo, Scripta Mater 181 (2020) 76–81.
- [19] Z. Zhao, H. Chen, H. Xiang, F.Z. Dai, X. Wang, W. Xu, K. Sun, Z. Peng, Y. Zhou, J. Adv. Ceram. 9 (2020) 303–311.
- [20] L. Chen, J. Guo, Y. Zhu, M. Hu, J. Feng, J. Am. Ceram. Soc. (2020).
- [21] L. Chen, Y. Wang, M. Hu, L. Zhang, J. Wang, Z. Zhang, X. Liang, J. Guo, J. Feng, Appl. Phys. Lett. 118 (2021), 071905.
- [22] J. Zhu, X. Meng, J. Xu, P. Zhang, Z. Lou, M.J. Reece, F. Gao, J. Eur. Ceram. Soc. 41 (2021) 1052–1057.
- [23] M. Qin, H. Vega, D. Zhang, S. Adapa, A.J. Wright, Q. Wang, Y.-T. Yeh, D. Zhang, M. Everett, J. Neuefeind, R. Chen, J. Luo, J. Adv. Ceram. 11 (4) (2022) 641–655, <https://doi.org/10.1007/s40145-022-0575-5>.
- [24] F. Li, L. Zhou, J.-X. Liu, Y. Liang, G.-J. Zhang, J. Adv. Ceram. (2019) 1–7.
- [25] Z. Teng, L. Zhu, Y. Tan, S. Zeng, Y. Xia, Y. Wang, H. Zhang, J. Eur. Ceram. Soc. (2019).
- [26] K. Ren, Q. Wang, G. Shao, X. Zhao, Y. Wang, Scr. Mater. 178 (2020) 382–386.
- [27] H. Junjie, H. Guo, L. Jing, T. Jingchao, J. Eur. Ceram. Soc. 41 (2021) 6080–6086.
- [28] L. Zhou, F. Li, J.X. Liu, Q. Hu, W. Bao, Y. Wu, X. Cao, F. Xu, G.J. Zhang, J. Eur. Ceram. Soc. 40 (2020) 5731–5739.
- [29] A.J. Wright, J. Luo, J Mater Sci 55 (2020) 9812–9827.
- [30] C.M. Rost, E. Sachet, T. Borman, A. Moballegh, E.C. Dickey, D. Hou, J.L. Jones, S. Curtarolo, J.P. Maria, Nat. Commun. 6 (2015) 8485.
- [31] S. Jiang, T. Hu, J. Gild, N. Zhou, J. Nie, M. Qin, T. Harrington, K. Vecchio, J. Luo, Scr. Mater. 142 (2018) 116–120.
- [32] J. Gild, Y. Zhang, T. Harrington, S. Jiang, T. Hu, M.C. Quinn, W.M. Mellor, N. Zhou, K. Vecchio, J. Luo, Sci. Rep. 6 (2016) 37946.
- [33] M. Qin, Q. Yan, H. Wang, C. Hu, K.S. Vecchio, J. Luo, Scr. Mater. 189 (2020) 101–105.
- [34] M. Qin, Q. Yan, Y. Liu, J. Luo, J. Adv. Ceram. 10 (2021) 166–172, <https://doi.org/10.1007/s40145-020-0438-x>.
- [35] M. Qin, Q. Yan, H. Wang, K.S. Vecchio, J. Luo, J. Eur. Ceram. Soc. 41 (2021) 2968–2973.
- [36] H. Chen, Z. Zhao, H. Xiang, F.Z. Dai, J. Zhang, S. Wang, J. Liu, Y. Zhou, J. Mater. Sci. Technol. 38 (2020) 80–85.
- [37] M. Qin, Q. Yan, Y. Liu, H. Wang, C. Wang, T. Lei, K.S. Vecchio, H.L. Xin, T. J. Rupert, J. Luo, J. Eur. Ceram. Soc. 41 (2021) 5775–5781.
- [38] J. Gild, J. Braun, K. Kaufmann, E. Marin, T. Harrington, P. Hopkins, K. Vecchio, J. Luo, Journal of Materiomics 5 (2019) 337–343.
- [39] S. Shivakumar, M. Qin, D. Zhang, C. Hu, Q. Yan, J. Luo, Scripta Mater 212 (2022), 114557.
- [40] T.J. Harrington, J. Gild, P. Sarker, C. Toher, C.M. Rost, O.F. Dippo, C. McElfresh, K. Kaufmann, E. Marin, L. Borowski, P.E. Hopkins, J. Luo, S. Curtarolo, D. W. Brenner, K.S. Vecchio, Acta Mater 166 (2019) 271–280.
- [41] X. Yan, L. Constantin, Y. Lu, J.F. Silvain, M. Nastasi, B. Cui, J. Am. Ceram. Soc. 101 (2018) 4486–4491.
- [42] E. Castle, T. Csanádi, S. Grasso, J. Dusza, M. Reece, Sci. Rep. 8 (2018) 8609.
- [43] A.J. Wright, Q. Wang, C. Huang, A. Nieto, R. Chen, J. Luo, J. European Ceram. Soc. 40 (2020) 2120–2129.
- [44] K. An, Y. Chen, A.D. Stoica, MRS Bull 44 (2019) 878–885.
- [45] J. Wu, X. Wei, N.P. Padture, P.G. Klemens, M. Gell, E. Garcia, P. Miranzo, M. I. Osendi, J. Am. Ceram. Soc. 85 (2002) 3031–3035.
- [46] J.E. Greedan, D. Gout, A.D. Lozano-Gorrin, S. Derahkshan, T. Proffen, H.-J. Kim, E. Božin, S.J.L. Billinge, 2022 (n.d.).
- [47] F.P. Marlton, Z. Zhang, Y. Zhang, T.E. Proffen, C.D. Ling, B.J. Kennedy, Chem. Mater. 33 (2021) 1407–1415.
- [48] B.J. Kennedy, J. Solid State Chem. 123 (1996) 14–20.
- [49] I.M. Gussev, E.C. O'Quinn, G. Baldinozzi, J. Neuefeind, R.C. Ewing, F. Zhang, M. Lang, Acta Mater 196 (2020) 704–709.
- [50] B. Jiang, C.A. Bridges, R.R. Unocic, K.C. Pitkic, V.R. Cooper, Y. Zhang, D.Y. Lin, K. Page, J. Am. Chem. Soc. (2021).